Journal Pre-proofs

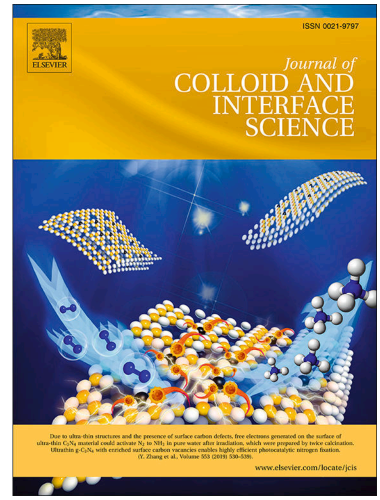

Regular Article

In-situ capillary pressure and wettability in natural porous media: Multi-scale experimentation and automated characterization using x-ray images

Ahmed Zankoor, Mahdi Khishvand, Abdelhalim Mohamed, Rui Wang, Mohammad Piri

PII:	S0021-9797(21)00926-7
DOI:	https://doi.org/10.1016/j.jcis.2021.06.052
Reference:	YJCIS 28245

To appear in: *Journal of Colloid and Interface Science*

Received Date:	30 March 2021
Revised Date:	8 June 2021
Accepted Date:	9 June 2021

Please cite this article as: A. Zankoor, M. Khishvand, A. Mohamed, R. Wang, M. Piri, In-situ capillary pressure and wettability in natural porous media: Multi-scale experimentation and automated characterization using x-ray images, *Journal of Colloid and Interface Science* (2021), doi: https://doi.org/10.1016/j.jcis.2021.06.052

In-situ capillary pressure and wettability in natural porous media: Multi-scale experimentation and automated characterization using x-ray images

Ahmed Zankoor*, Mahdi Khishvand, Abdelhalim Mohamed, Rui Wang, and Mohammad Piri

Center of Innovation for Flow through Porous Media, Department of Petroleum Engineering, University of Wyoming, Laramie, WY 82071, USA.

Abstract

Hypothesis. Geometrical analyses of pore-scale fluid-fluid-rock interfaces have recently been used for in-situ characterization of capillary pressure and wettability in natural porous media. Nevertheless, more robust techniques and multi-scale, well-characterized experimental data are needed to rigorously validate these techniques and thereby enhance their efficacy when applied to saturated porous media.

Experiments and Image analysis. We present two new techniques for automated measurements of in-situ capillary pressure and contact angle, which offer several advancements over previous methodologies. These approaches are methodically validate using synthetic data and x-ray images of capillary rise experiments, and subsequently, apply them on pore-scale fluid occupancy maps of a miniature Berea sandstone sample obtained during steady-state drainage and imbibition flow experiments.

Findings. The results show encouraging agreement between the image-based capillary pressure-saturation function and its macroscopic counterpart obtained

*Corresponding author
Email address: azankoor@uwyo.edu (Ahmed Zankoor)

from a porous membrane experiment. However, unlike the macroscopic behavior, the micro-scale measurements demonstrate a nonmonotonic increase with saturation due to the intermittency of the pore-scale displacement events controlling the overall flow behavior. This is further explained using the pertinent micro-scale mechanisms such as Haines jumps. The new methods also enable one to generate in-situ contact angle distributions and distinguish between the advancing and receding values while automatically excluding invalid measurements.

Keywords: Porous media, In-situ capillary pressure, Wettability, Interfacial curvature, Imaging, Imbibition.

---

1. Introduction

Porous media occupied by immiscible fluids are encountered in numerous engineering applications including soil science, oil and gas recovery, geologic sequestration of CO_2, and food processing. Such multi-phase systems are characterized by the existence of pore-scale interfaces that separate different phases from each other. Fluid configurations and flow behavior in the pore space, under both static and dynamic conditions, are strongly influenced by the characteristics of these interfaces. Among the relevant interfacial properties, contact angle and fluid-fluid interfacial curvature are of special interest. The first parameter is the universal measure of the wettability of a solid surface, and the latter can be used to quantify the local capillary pressure (i.e., pressure jump across a meniscus) values using the Young-Laplace equation [1, 2]:

$$P_c = P_{NW} - P_W = \sigma \times K_T \tag{1}$$

where P_c is the capillary pressure, P_{NW} and P_W refer to, respectively, the pressures of the non-wetting and wetting phases across that interface, σ denotes the interfacial tension between the two fluids, and K_T is the total curvature of the interface, i.e., the sum of the principal curvatures.

Various experimental techniques have been developed to quantify the above-mentioned properties, such as the sessile drop/captive bubble method for contact angle measurement [3], and porous plate and mercury intrusion techniques [4, 5, 6] for capillary pressure characterization. These experimental methods have been widely recognized as valuable in characterizing the macroscopic fluid-fluid and solid-fluid properties. Nonetheless, these approaches are unable to capture micro-scale properties and hence, considerable attention has recently been directed towards in-situ (i.e., pore-scale) measurements of the multiphase interfacial properties.

The advent of non-destructive imaging techniques, namely x-ray computed tomography, in the past two decades has allowed the visualization of fluid-fluid-solid interfaces inside porous media and opened a window of opportunity to quantify the characteristics of multiphase systems (e.g., in-situ contact angle and curvature) directly from high-resolution fluid occupancy maps. Analyzing these pore-scale images provides several advantages over the traditional macro-scale methods. For instance, unlike the conventional techniques, in-situ contact angle measurements reflect the impacts of mineral heterogeneity and roughness on wettability; or the use of in-situ (i.e., local) capillary pressure characterization instead of an average macroscopic capillary pressure, obtained using conventional methods, enables one to interpret local fluid displacement and entrapment behavior. These improvements have created an avenue for conducting advanced multi-phase studies at the pore-scale that can shed more light on complex subtleties of flow physics. Such achievements, however, require the development of (i) robust experimental platforms to generate pore-scale images during flow processes, and (ii) computational platforms to analyze the images and estimate in-situ interfacial properties. Image analysis techniques for in-situ contact angle measurements have been developed based on geometric analysis of the fluid-fluid and fluid-solid interfaces (FFI and FSI, respectively). The contact angles can be measured at any point where the FFI and FSI meet each other. This set of individual points are collectively referred to as three-phase contact lines (TCL). To measure contact angle at each point, one needs to first find a unique plane whose normal is parallel to the TCL at that point, and then measure the angle between the FFI and FSI in that specific plane. Several studies have applied semi-manual analysis techniques to measure in-situ contact angles in pore-scale investigations of water-wet [7, 8, 9] and oil-wet systems [10, 11]. These approaches, however, are limited by the number of measurements and the difficulties in finding TCL and determining the contact angle planes.

The previously mentioned limitations have driven researchers to develop automated techniques to measure contact angles using different geometry-based approaches. The automated methods use voxel- or pixel-connectivity [12, 13, 14], mesh-based [15], or a level set methods [16] to identify the FFI, FSI, and the triple contact points (TCP). Thereafter, the contact angles can be measured at the TCP using i) planes or circles and lines fitted to the pixels of the FFI and FSI or ii) normal vectors at the meshes of the FFI and FSI. These techniques have mitigated most of the limitations associated with manual measurements. Nevertheless, the measurements could still be subjected to significant uncertainties since they are performed at any locations along the TCL without employing screening criteria to exclude erroneous measurements.

Pore-scale fluid occupancy maps can also be used to calculate the curvature of FFIs during various flow processes and thereby characterize the local capillary pressures (e.g. [17, 18, 19, 20, 21]). This is mostly done through a patch fitting method, in which the smoothed interfaces are locally fitted with a quadratic surface equation. Thereafter, the principal curvatures can be calculated analytically and then be used to estimate the local capillary pressures from Equation (1). This method is relatively insensitive to noises and hence, has been frequently used for complex interfaces extracted from micro-CT images of porous media. However, it involves a user-tunable parameter corresponding to the size of the neighborhood over which the curvature at a vertex (i.e., a point on a discrete surface) is calculated. Small neighborhood values result in significant uncertainties in curvature calculations and cause the algorithm to become unstable, and large values lead to overlooking the local variations in curvature for small features, e.g., at arc terminal menisci (AMs).

Among the studies that used interfacial curvature analysis, there have been several attempts to assess the relationship between the macroscopic and microscopic capillary pressures. Nonetheless, these comparisons have been either made with synthetic well-sorted porous media [17, 22], impacted by interface relaxation (due to halting of the flow) as well as capillary end-effects [19], or obtained only for an imbibition process and within a narrow range of saturation values [23].

The existing literature on in-situ contact angle and capillary pressure measurements has significantly enriched our understanding of the multiphase flow phenomena in the pore space. Nevertheless, there are multiple issues, as discussed above, that need to be addressed and appropriately resolved. These shortcomings motivated us to develop two new platforms, i.e., automated curvature measurement (ACM) and contact angle measurement (ACAM), for the characterization of geometrical properties of interfaces that incorporate various image analysis improvements to minimize the uncertainties associated with the use of automated techniques for natural porous media. The ACM and ACAM platforms were then validated using different synthetic surfaces with well-known curvatures. The accuracy of the ACM platform was further evaluated by calculating curvature-based capillary pressures from micro-CT images generated during a set of capillary rise experiments and comparing these results with those obtained from measuring the height of the capillary rise. After these validation stages, two series of flow experiments were carried out at different scales to generate well-characterized experimental data needed to assess the efficacy of the platforms when applied to natural porous media. Specifically, the ACM technique was applied to micro-CT images obtained during steady-state drainage and imbibition experiments conducted on a miniature Berea sandstone core to measure local capillary pressures and characterize the in-situ wettability. The steady-state approach enabled us to cover a wide range of saturation values, and the use of continuous injection while imaging minimized interface relaxation. The local capillary pressures were then compared against the macroscopic capillary pressure-saturation function obtained from a porous membrane experiment performed on a companion Berea sandstone core plug. The differences between the local and macroscopic capillary pressures are explained based on pore-scale displacement events.

In the following sections, we first describe the materials and methods for the capillary rise and the micro- and macro-scale core-flooding experiments and discuss the workflow of the ACM and ACAM platforms in detail. This is then followed by examining the accuracy of the platforms using synthetic data and the information obtained from the capillary rise experiments. Finally, in the last section, the application of these platforms on the micro-CT images of natural porous media is discussed. We also present the comparison between the micro- and macro-scale capillary pressure data and discuss several related insights.

2. Materials and methods

In this section, we briefly discuss the materials used and the experimental procedures adopted to carry out the capillary rise and steady-state micro-scale flow experiments. This is followed by a brief description of the core-scale experiment performed to obtain the macro-scale capillary pressure-saturation relationship for the Berea sandstone. A detailed description of the fluids, experimental apparatuses, experimental procedures, and image pre-processing procedures is available in the Supplementary Information. Finally, the algorithms that have been developed and implemented within the ACM and ACAM platforms are described in Sections 2.1.1 and 2.1.2.

2.1. Experiments

2.1.1. Capillary rise experiments

In a capillary rise experiment, the capillary height is proportional to the curvature of the fluid-fluid interface, and both can be used to independently calculate the capillary pressure. Hence, the capillary height was utilized as a tool to validate estimates obtained from the ACM platform. To this end, several capillary rise experiments were performed using glass capillary tubes with circular cross-sections (obtained from Friedrich and Dimmock Inc.) while different liquid phases and air were used as the wetting and non-wetting phases, respectively[24]. The fluid-fluid interface in each experiment was imaged using a micro-CT scanner, and the images were subsequently analyzed using the ACM platform to calculate their respective curvature and capillary pressure. The curvature-based capillary pressures were compared against their height-based counterparts to determine the accuracy of the interfacial curvature measurements. The above-mentioned procedure was repeated twice or more for each fluid pair (Table 1) at various image resolutions.

2.1.2. Micro-scale core-flooding experiments

The micro-scale two-phase flow experiments were performed on a miniature core sample at elevated pressure and ambient temperature using a high-pressure multiphase core-flooding system integrated with a micro-CT imaging system. The rock sample was a water-wet Berea sandstone with diameter, length, porosity (determined from the x-ray images), and absolute brine permeability of 4.9 mm, 71.5 mm, 18.5%, and 8.51×10^{-13} m^2 (862 mD), respectively. The non-wetting and wetting fluids were purified Soltrol 170 and brine with 2 wt.% $CaCl_2.6H_2O$ and 7 wt.% NaI. The flow tests included multiple steady-state drainage steps to establish an irreducible water saturation (S_{wi}) followed by several steady-state imbibition processes to reach the waterflood residual oil saturation (S_{orw}). At the end of each flow step, the sample was imaged to map the pore-scale fluid occupancy [25, 26]. The micro-CT images were processed using Avizo software and then the ACM platform to measure the saturation data, and local curvatures (i.e., micro-scale local capillary pressures).

2.1.3. Macro-scale capillary pressure measurement (porous membrane experiment)

The porous membrane experiment was conducted to obtain the drainage capillary pressure-saturation curve of Berea sandstone, which was later compared against the in-situ local capillary pressures of the micro-scale core-flooding tests. The experiment was performed by applying multi-stage constant pressure conditions on a core sample with a diameter, length, porosity (measured using an automated Helium-porosimeter), and absolute brine permeability of 38.1 mm, 76.2 mm, 21.5 %, and 6.66×10^{-13} m^2 (675 mD), respectively. A hydrophilic porous membrane was placed in capillary contact with the outlet face of the core sample, which only allowed the aqueous phase to pass through it as the oil phase was introduced into the sample. The non-wetting and wetting fluids were purified Soltrol 170 and brine with 2 wt.% $CaCl_2.6H_2O$, respectively. The core sample was first fully saturated with the aqueous solution, and then subjected to a multi-stage unsteady-state drainage process using Soltrol 170. This process involved step-wise increases in the injection pressure by adjusting the height of the Soltrol reservoir. At each stage, the produced brine was received in a container to calculate the saturation using the material balance technique, and the hydrostatic head and transducer readings were used to calculate the respective capillary pressure.

2.2. Image analysis platforms

The segmented micro-CT images were imported into the ACM and ACAM platforms, developed in MATLAB, to obtain the curvature and contact angle information, respectively. The main steps of the ACM and ACAM workflows are shown in Figure 1 (examples in Figure S3). As mentioned earlier, the methodology adopted in this study includes several improvements over the previous ones to better address and minimize the uncertainties associated with in-situ measurements of capillary pressure and contact angle from micro-CT images of natural porous media. In the ACM platform, we used a technique based on the fundamental forms of differential geometry to calculate the curvature, which is known to be more accurate than the quadratic fit method in detecting local variations of the surface topology [27]. The capability of the platform was enhanced to detect and, if necessary, eliminate the features that could result in nonrepresentative interfacial curvatures. These include (i) wetting layers residing along grain surfaces, (ii) the peripheral ring of the fluid-fluid interfaces, i.e., the fluid-fluid interface vertices located at or near the triple contact points, and (iii) the small patches of FFIs generated due to the presence of minuscule oil globules. In the meantime, the small interfaces such as arc menisci were preserved, and their curvature values can be calculated. For the ACAM platform, the TCL was extracted using a new mesh-based approach based on the edges of the FFI, which is presumably more effective than the voxel-based and mesh-based approaches presented in the literature. In addition, several screening criteria were set to automatically exclude the erroneous contact angle measurements associated with insufficient fluids contact (i.e., poor interfaces) and image artifacts.

2.2.1. Curvature analysis

For curvature analysis, the fluid-fluid interfaces were first extracted from the 3D segmented images, and subsequently smoothed to reduce pixelation effects. Thereafter, the surface curvature was computed at each point (i.e., vertex) by applying a method based on the fundamental forms of differential geometry as described by Rusinkiewicz (2004)[27]. This approach uses the smallest possible neighborhood (i.e. one ring of faces around each vertex) and is more stable, robust, and sensitive to local curvature variations than the patch fitting method discussed earlier. This capability is assumed to be crucial in characterizing small features, such as arc terminal menisci (AMs) at high capillary pressures. The curvatures of vertices over each specific surface were arithmetically averaged to calculate the corresponding local capillary pressure using the Young-Laplace equation. We have also developed multiple criteria to reduce the uncertainties associated with curvature analyses from pore-scale images of natural porous media. The details of the various steps taken during the curvature analysis are described below.

Extracting interfaces. The program first reads the segmented images (i.e., labeled data file exported from Avizo software) and rebuilds/reforms the 3D volume of the phases. The oil-brine interfaces are then extracted using the Marching cubes algorithm to generate a polygonal mesh of the FFI, which consists of triangles that cut through the voxels. The coordinates of the triangles vertices are obtained by interpolating between the coordinates of the surrounding voxel [28]. The extracted surface is defined as a triangular mesh M, which consists of a set of distinct vertices $V = v_i \in \mathbb{R}^3$, edges $E = e_{ij} \in V^2$, and faces $F = f_{ijk} \in V^3$. The extracted mesh is formed of consistently oriented faces, so that the normal vectors to the surfaces always point from one phase to another.

Smoothing fluid-fluid interfaces. The FFIs generated in the previous section should be smoothed to reduce the impact of image voxelization on the curvature analysis. This process is crucial since performing curvature analysis on surfaces that are insufficiently smoothed will result in estimates with a significant degree of fluctuation. On the other hand, over-smoothing the FFIs may deform the surface by eliminating small features or shrinking the surface area. In this study, the mesh of the fluid-fluid interfaces (i.e., M) was smoothed using an implicit fairing method described by Desbrun et al.[29] and implemented by Kroon[30]. The computed surface curvature is inherently dependent on the number of smoothing iterations. It was found that 15 smoothing iterations was an optimum value to be used in the platform. For more details please see the Supplementary Information.

Curvature calculation. After a smoothed representation of the interface is obtained, we employ an algorithm for estimating the curvature values at each vertex of the interface using the fundamental forms of differential geometry[27, 31]. In this section, a brief overview of this approach is explained[27, 32, 33, 34, 35]. As shown in Figure 2, a three-dimensional continuous surface $\mathbf{S}$ can be expressed in terms of the position vector $\mathbf{r}$ and the two parameters u and v by the vector equation:

$$\mathbf{r} = \mathbf{f}(u, v) = \phi(u, v)\mathbf{i} + \psi(u, v)\mathbf{j} + \chi(u, v)\mathbf{k} \tag{2}$$

To define an arbitrary curve γ on $\mathbf{S}$, both u and v should be defined as functions of a third single parameter t. In this way, the representation of γ by Equation(2) can be recast as:

$$\mathbf{r} = \mathbf{f}(t) = \phi(t)\mathbf{i} + \psi(t)\mathbf{j} + \chi(t)\mathbf{k} \tag{3}$$

A tangent vector to γ at any point P on the surface is then given by the total derivative:

$$\frac{d\mathbf{r}(u,v)}{dt} = \mathbf{r}_u \frac{du}{dt} + \mathbf{r}_v \frac{dv}{dt} \tag{4}$$

where $\mathbf{r}_u$ and $\mathbf{r}_v$ are the partial derivatives of $\mathbf{r}$ with respect to u and v, respectively, and they are tangent vectors to the parametric curves at P. The parametric curves are obtained when one parameter (e.g., u or v) is changing while the other one is constant, such as the latitude and longitude for a sphere. A particularly useful choice for the parameter t is the arc length of the curve s since it arises naturally from the shape of the curve and is independent of the chosen coordinate system. Specifically, if the curve γ is parameterized with respect to its arc length s then Equation(4) will define a unit-tangent vector $\mathbf{t}$ to γ at P: $\mathbf{t} = \frac{d\mathbf{r}}{ds} = \mathbf{r}_u p + \mathbf{r}_v q$, where $p = \frac{du}{ds}$ and $q = \frac{dv}{ds}$. Note that Equation(4) shows that $\frac{d\mathbf{r}}{ds}$ lies in the span of $\mathbf{r}_u$ and $\mathbf{r}_v$, which is referred to as the tangent plane $\mathbf{T_p}$ to the surface $\mathbf{S}$ at P (see Figure 2). The unit-normal $\mathbf{n}$ to $\mathbf{T_p}$ at P which is also normal to the surface $\mathbf{S}$ at P can be found from the following equation:

$$\mathbf{n} = \frac{\mathbf{r}_u \times \mathbf{r}_v}{\mid \mathbf{r}_u \times \mathbf{r}_v \mid} \tag{5}$$

The plane spanned by $\mathbf{n}$ and $\mathbf{t}$ intersects with $\mathbf{S}$ in a curve that is referred to as a normal section. The normal curvature K_N of $\mathbf{S}$ at P in the direction of $\mathbf{t}$, is defined as the reciprocal of the radius of the circle that best approximates this normal section and can be calculated by:

$$K_N = \begin{pmatrix} p & q \end{pmatrix} \begin{pmatrix} L & M \\ M & N \end{pmatrix} \begin{pmatrix} p \\ q \end{pmatrix} = \begin{pmatrix} p & q \end{pmatrix} \mathbf{II} \begin{pmatrix} p \\ q \end{pmatrix} \tag{6}$$

where $L = -\mathbf{n}_u \cdot \mathbf{r}_u$, $M = -(\mathbf{n}_v \cdot \mathbf{r}_u + \mathbf{n}_u \cdot \mathbf{r}_v)/2$, $N = -\mathbf{n}_v \cdot \mathbf{r}_v$, and $\mathbf{n}_u$ and $\mathbf{n}_v$ represent the directional derivatives of the surface unit normal $\mathbf{n}$. The symmetric matrix $\mathbf{II}$ is called the second fundamental tensor. Equation(6) can be used to calculate the curvature of $\mathbf{S}$ at P along any arbitrary normal section (i.e., in the direction of any $\mathbf{t}$).

Among the infinite number of normal sections, the two with minimum and maximum curvatures are of special interest. These curvatures are referred to as the principal curvatures, K_1 and K_2, and are inherently orthogonal to each other. These principal curvatures and their directions (at P on surface $\mathbf{S}$) can be found from the eigenvalues and eigenvectors of $\mathbf{II}$, respectively. It should be noted that $\mathbf{II}$ is a characteristic property of the surface at any point and has no reference to any specific curve on the surface. Conventionally, the sum and product of the two principal curvatures are called the total and Gaussian curvatures, respectively (i.e., $K_T = K_1 + K_2$ and $K_G = K_1 \times K_2$).

Unlike for analytical surfaces, the matrix $\mathbf{II}$, and hence the principal curvatures, cannot be directly calculated for discrete surfaces, which are formed by vertices surrounded by several triangular faces. Therefore, Rusinkiewicz [27] used a finite difference approach to estimate the second fundamental tensor of discrete surfaces at any vertex and then calculate the corresponding principal curvatures. A more detailed illustration of the steps followed in this approach can be found in the Supplementary Information.

2.2.2. In-situ contact angle measurement

The main steps of the ACAM workflow are demonstrated in Figure 1 and are outlined as follows:

Extracting three-phase contact lines. The ACAM platform uses a mesh-based approach to extract the oil-brine-solid contact points. We developed a technique to first identify the boundary edges of the fluid-fluid interface mesh, and then trace the connectivity of the vertices of these edges in the 3D space to obtain the triple contact line (TCL). The resulting TCL segments are then smoothed using a moving average procedure. This approach is assumed to be computationally less expensive than the voxel-based approaches [13] where the TCL is generated by examining every voxel of a fluid phase, and selecting the voxels that neighbor both the other fluid and the solid phases through either faces (6-connectivity), edges (18-connectivity), or vertices (26-connectivity). Moreover, these voxel-based techniques often eliminate some parts of the TCL if face-connectivity is used, or lead to unrealistically complicated TCL when edge- or vertex-connectivity is used.

Generating contact angle planes. As discussed earlier, the contact angle at a given point A on the TCL can only be measured in a plane that is perpendicular to the TCL at that point. To generate this contact angle plane, the program first traces successive points (in the proximity of point A) on the smoothed TCL and uses their coordinates to define a tangent vector to the TCL. This vector along with the coordinates of point A are used to generate the contact angle plane at point A, as shown in Figure 3(a). This procedure is repeated for all points on the TCL. The 2D contact angle planes are then processed to find the fluid-fluid, fluid-solid interfaces as well as the three-phase contact points. Since the slice may contain different segments of these pixels, the pixels next to the selected TCL pixel are traced and selected, as shown in Figure 3(b).

Measuring contact angle. To measure the contact angle at a target point on the TCL, a surrounding sub-slice (a few pixels) is initially examined to identify the fluid-solid and fluid-fluid pixels near that point. The program then uses a straight line to approximate the solid surface locally, and the FFI pixels are used to find the tangent to the fluid-fluid interface through either a circle- or line-fitting method. In the circle-fitting method, the fluid-fluid pixels found in the larger 2D slice (i.e., the entire contact angle plan) are fitted with a circle and the tangent to this circle at the TCL point is considered as the fluid-fluid line. In the line-fitting method, however, the fluid-fluid line is the line that interpolates through the FFI pixels in the sub-slice. The angle between the FFI and FSI is measured through the denser phase and reported as the contact angle. The contact angles are referred to as circle-line or two-line CA when either the circle- or line-fitting method is used to approximate the FFI pixels, respectively. In general, we found that the estimated contact angles using the two-line CA method are more representative than the circle-line method, since, in many cases, the circle fitted to the fluid-fluid pixels is incorrect.

Screening the data. To address the complexity of the configurations observed from many slices (caused by the irregularity of the pore space, segmentation errors, fluid layers along the solid edges, etc.), we utilize an acceptance criterion to identify the slices that produce accurate contact angle estimates. Such slices are required to include fluid/solid phases with sufficient contact. This is achieved by specifying a minimum number of fluid-fluid and fluid-solid pixels that must be present in the analyzed slice or sub-slice. The platform rejects any slices that do not meet this requirement. Examples of the rejected slices are shown in Figure S8.

3. Results and discussion

In this section, we briefly discuss the validation of the platforms using synthetic data and the uncertainty associated with curvature analysis for MTM and AM's interfaces. This is then followed by a comparison between the capillary pressures calculated from the hydrostatic head and those computed from the micro-CT images for the capillary rise experiments to further validate the ACM platform. After the initial validation studies are discussed, we present the in-situ capillary pressure and wettability data generated using the platforms with the micro-CT images of the miniature core-flooding experiments. The curvature-based capillary pressures are also compared against the macroscopic capillary pressure data from the porous membrane experiment and the consistencies/variations are substantiated based on the pore-scale observations.

3.1. Synthetic images

3.1.1. Curvature calculation

The ACM platform was initially applied on multiple surfaces of known analytical curvatures. The first example was a catenoid, which has analytical Gaussian curvatures ranging from -1 to 0 along the major axis of symmetry [36]. The catenoid surface was created using (i) a discretized version of the analytical equation or (ii) voxelated 3D volume rendering. The computed curvatures for the catenoid surfaces were either identical (in the case of type (i) surfaces) or very close (for type (ii) surfaces) to their analytical counterparts. To better depict realistic fluid-fluid interface morphologies in the pore space, we also generated 3D rendered volumes of wetting and non-wetting phases in a triangular capillary tube while the main terminal and arc menisci (MTM and AMs) were present in the center and corners of the tube, respectively [37]. The computed MTM curvatures always stay in agreement with the analytical value. For the AMs, however, and particularly at higher non-wetting phase saturations, the computed values deviate from the analytical counterpart. This is because, as the non-wetting phase saturation increases, the AMs move further towards the corners and occupy fewer voxels. Hence, in these regions, the extracted surface is too small and a greater degree of uncertainty in the smoothing and curvature calculation steps is present.

3.1.2. Contact angle measurement

The accuracy of the contact angle measurement algorithm was tested by measuring contact angles for a 3D voxelized droplet residing on a solid surface. The contact angles were measured multiple times while the relative position of the droplet and the solid surface varied from one case to another (i.e. to obtain different contact angles). For each case, the 3D volume was analyzed according to the workflow presented in Figure 1, and the computed contact angles were compared against the analytically calculated values. The results showed that the contact angles measured using both the two-line and circle-line methods agree within $3°$ with the analytical calculations. A more detailed discussion of the validation of both platforms using synthetic data can be found in the Supplementary Information.

3.2. Capillary rise experiment

To further validate the ACM platform, this platform was also applied to the micro-CT images acquired during the capillary rise experiments. Each grayscale image was first segmented using Avizo software and then processed by the ACM platform to extract the fluid-fluid interface and compute the average curvature for the interface between each pair of fluids. For each experiment, the capillary height was measured using a cathetometer and the contact angle was obtained from image analysis.

For capillary rise experiments in circular capillary tubes there are three equivalent representations of the capillary pressure:

$$P_c = \underbrace{\frac{2\sigma\cos\theta}{r}}_{\textbf{(I)}} = \underbrace{\sigma\kappa_T}_{\textbf{(II)}} = \underbrace{\Delta\rho g h}_{\textbf{(III)}} \tag{7}$$

where P_c is the capillary pressure in N/m^2 (Pa), r is the radius of the capillary tube (m), θ and σ are the contact angle (degrees) and surface tension (N/m), respectively, κ_T denotes the total curvature (i.e., the sum of the principal curvatures) of the interface (1/m), $\Delta\rho$ is the density contrast (Kg/m^3), g stands for the gravitational acceleration (approximately 9.81 m/s^2), and h refers to the capillary height (m). The information in Table 1 and Table S2 can readily be used in expressions Pc_{I} - Pc_{III} of Equation(7) to calculate three different estimates of the capillary pressure. The comparison between the results in Figure 4 reveals that, for most of the cases, the capillary pressure calculations based on the interfacial curvature (i.e.,Pc_{II}) are in good agreements with the corresponding calculations from the other equations, i.e., Pc_{I} and Pc_{III}. Specifically, these results reveal variations of less than 5% in relative error (i.e., $\frac{|Pc_{\mathrm{II}}-Pc_{\mathrm{I}or\mathrm{III}}|}{0.5(Pc_{\mathrm{II}}+Pc_{\mathrm{I}or\mathrm{III}})} \times 100\% < 5\%$) for the brine and Soltrol experiments, whereas for the mixture of brine and glycerol, the relative errors are relatively higher (approximately 15%). The uncertainty in the latter case is attributed to the thick transition zones [24] that were observed close to the fluid-fluid interfaces in the micro-CT images which introduced uncertainties into the image segmentation as well as contact angle and curvature measurements. This finding highlights the critical role of improved image contrast in generating high-quality in-situ capillary pressure data.

3.3. Core-flooding experiments: capillary pressure quantification

3.3.1. Macro-scale porous membrane experiment

As discussed earlier, the porous membrane experiment was conducted to generate the macroscopic capillary pressure function for an oil-displacing-brine process in a Berea sandstone sample. Figure 5 provides a comparison between the capillary pressure-saturation relationship obtained in this study with that reported by Raeesi et al. (2014)[38]. To account for variations in the rock and fluid properties, the latter data set was normalized (using the Leverett J-function) against the first capillary pressure data set [5]. The oil-water contact angle for this study was measured (using the ACAM platform) to be approximately 50 degrees while for the gas-water system of Raeesi et al.[38], the contact angle was assumed to be 35 degrees [8]. Figure 5 shows close consistencies between the results of both experiments. As the non-wetting phase pressure increases, the oil (gas) menisci located at the entry of pores and throat invade into the pore elements depending on the accessibility of oil to the pores and the respective threshold capillary pressures and displace the wetting phase toward the production side. At the initial stages, the wetting-phase saturation decreases significantly with slight increases in capillary pressure. When most of the pores are at least partially oil-filled, the water saturation changes mostly due to the movement of AMs toward the corners and invasion of oil into crevices and small pores. Hence, the Pc-Sw plot suddenly ascends, meaning a higher incremental oil pressure is required for a given change in the water saturation.

3.3.2. Microscopic capillary pressure: Measurement approach

As mentioned previously, the capillary pressure-saturation relationship can also be generated from the pore-scale fluid occupancy maps obtained during the drainage (D1-D13) and imbibition (I1-I6) flow processes conducted on the miniature Berea sandstone sample. The flow conditions and saturation data for the macro- and micro-scale experiments can be found in the Supplementary Information. The pore-scale fluid occupancy map obtained during each stage of the flow processes was subsequently used for curvature analysis using the following procedure:

- Separating the connected oil phase: We first separated the connected non-wetting phase clusters, which control the macroscopic capillary pressure of the system. This step was particularly essential for the imbibition processes where a significant amount of oil could be trapped due to pore-scale displacement events such as snap-off.
- Improving the ACM platform for complex interfaces: The complexity of fluid-fluid interfaces in micro-CT images of natural porous media often introduces notable uncertainties to curvature analysis results. Mainly, water films residing between the oil and grain can be captured as FFIs with curvatures that resemble those of the grain. Such wetting films were mostly removed from the segmented images by applying a seeded watershed segmentation algorithm or using Nagao and Majority filters of Avizo software. Moreover, the first peripheral rings of the fluid-fluid interfaces were excluded from the measurements because the curvature values of the edge vertices are always impacted by fluid-fluid-solid interfacial forces and hence introduce high uncertainties [23, 22, 36]. In addition to the wetting films and edge vertices, small patches of FFIs (generated due to segmentation errors or the presence of minuscule oil globules) may also lead to incorrect curvature computation and nonrepresentative local capillary pressures. Thus, the code was improved by including a module, which identified the disconnected patches[39], and discarded them if their sizes were below a certain cutoff value. Although thousands of FFI patches were found with few triangular faces, this process was generally skipped since it was computationally expensive, and the impact of those patches was found to be insignificant in this study. Examples of these image analysis steps can be found in the Supplementary Information(Figure S10).
- Implementing curvature analysis: The image stack for each flow stage was partitioned into four sub-volumes, each with a volume greater than the saturation-based representative elementary volume of Berea sandstone.

The image compartments were then analyzed in parallel using several computing processors [40]. We also employed MEX functions in MATLAB that call a C/C++ program for analysis [41], and hence further boosted the computational performance of the platform. This allowed an image with dimensions of 1980×2000×1700 voxels to be analyzed in less than 15 minutes using a 12-core processor.

The computed per-vertex curvature values during each flow stage formed a distribution with mostly positive values. The negative values, as observed in other studies [17, 18, 19, 23], are not physically expected in a water-wet system and can likely be attributed to the discrete nature of micro-CT images, wetting films on the rock surfaces, segmentation errors due to the presence of clays, and inaccuracies in mapping small pore elements due to the limited image resolution, all of which are inherently associated with micro-CT images of natural porous media. For the conditions of this study, the negative values were excluded, and the arithmetic average of the positive per-vertex curvatures was used to calculate the respective capillary pressure for the target sub-volume (e.g., Figure S11).

3.3.3. Microscopic capillary pressures: Drainage and imbibition

The average total curvature values obtained for various sub-volumes were used to calculate the local capillary pressures (using Equation 1) during each flow stage of the micro-scale core-flooding experiment. The image-based (i.e., local or micro-scale) capillary pressures and saturations for the drainage flow process are plotted in Figure 5 along with the macro-scale capillary pressure functions obtained from the porous membrane experiments. As seen in these figures, there is a strong correlation between the two cases and the general trends are similar; however, some inconsistencies are evident that can be mostly explained based on the pertinent pore-scale displacement mechanisms and their relationships with local capillary pressures.

At the outset of the experiments, the macro- and micro-scale capillary pressures are closely consistent with each other. As the drainage process continued, the macroscopic capillary pressure constantly increased (by increasing the Soltrol hydrostatic head in the porous membrane experiment or oil/water fractional flow in the miniature core-flooding test), while local capillary pressures changed in a different manner and through one of the following scenarios:

(i) If an interface existed at the center of a large pore, increases in macroscopic capillary pressure are likely to push the oil towards the corners or other connected pores with smaller diameters. Both processes result in interfaces with higher curvatures and local capillary pressures, which is consistent with changes in the macro-scale capillary pressures.

(ii) The above-mentioned mechanism could also occur for oil clusters near the corners of the invaded pores. An example of this type of change in local capillary pressure for an AM is demonstrated in Figure 6.

(iii) If the interface was located close to a narrow restriction (e.g., the throat in Figure 6(a), an increase in the macroscopic capillary pressure might cause the interface to invade into larger pores (as seen in 6(b)), which in turn led to interface relaxation, and a drop in the local capillary pressure. This event is mostly associated with the Haines jump during drainage [42, 43].

Figure 5 shows that during the early stages of the drainage process (i.e., oil saturation of up to 0.5), the two capillary pressure functions are in good agreement. This is because in this region, mechanism (i) was responsible for the displacement process and the oil phase invaded into a network of connected pores. However, at intermediate ranges of oil saturation (i.e., $0.5 < \mathrm{So} < 0.7$) increases in the microscopic capillary pressures are significantly smaller than their macroscopic counterparts. This occurs when most of the interconnected large pores were partially oil-filled, and further increases in the injection pressure would move the oil phase from narrow restrictions into water-filled intermediate-sized pore elements, and lead to drops in some local capillary pressures. It is believed the significant number of such invasion events (i.e., mechanisms (iii)) in these stages might have generated locally relaxed interfaces and made the local capillary pressures notably smaller than the corresponding, continuously increasing macroscopic capillary pressures.

Finally, during the later stages of the drainage process when most of the pores were at least partially oil-filled the pore-scale events (i) and (iii) were less frequent and most of the interface movements were thought to be governed by type (ii) events. Hence, as Figure 5 illustrates, increases in all local capillary pressures were observed as the oil/water fractional flow (i.e., macroscopic capillary pressure) was increased. The sharp slope of the graph in this region which implies the small amount of water production as the capillary pressure increases and is a typical characteristic of AM movements in capillary systems further corroborates the dominance of the AM movement mechanism. It is important to emphasize that near the end of the drainage process, interfaces were pushed toward the corners and could be partially lost or become too small and hence introduce large uncertainties into the measurements (see Section 3.1.1).

The previous discussion suggests that the macroscopic capillary pressure-saturation function would not necessarily be reflected at each interface in the porous medium due to the variety of pore-scale displacement events. The correlation between the capillary pressures might have also been impacted by the nonuniform distribution of curvatures in pores of various sizes. In other words, the interfaces in large pores could have possessed capillary pressures that are different than those in smaller pores. To further investigate this hypothesis, a sub-volume of the segmented image from drainage process D7 (with a size of $1980\times2000\times200$ voxels) was divided into 4 sub-volumes. For each sub-volume, the pore elements first separated and categorized under three classes of small (smaller than 5×10^5 voxels), intermediate (5×10^5 voxels $<$ pore size $< 2\times10^6$ voxels), and large (greater than 2×10^6 voxels) pores. Afterward, curvature analysis was performed on each group and the corresponding average capillary pressures were calculated. As depicted in Figure 8, the curvature values of the interfaces occupying small pores are generally higher than those in the larger pores. This is in line with the assumption that larger pores are more prone to be occupied by relaxed interfaces. This finding implies that a pore size-based curvature calculation is a promising approach to minimize the gap between the microscopic and macroscopic capillary pressures. This idea along with other potential solutions (e.g., more accurate smoothing algorithms) will be investigated in future studies to further enhance the correlation between the macro-scale and pore-scale capillary pressures.

The ACM platform was also applied to the segmented images of the imbibition process. Images obtained during the imbibition experiment were found to have sharper interfaces, and therefore their curvatures were easier to compute, than the images obtained during the drainage experiments. Hence, the uncertainty associated with the curvature calculation is believed to be smaller. Furthermore, the local capillary pressures for the imbibition process, presented in Figure 9, show more uniform values for various sub-volumes. As the imbibition process commenced, the AM and MTM interfaces hinged at their locations, and the contact angles moved from receding toward advancing values. This was also accompanied by a significant drop in local capillary pressures while only slight changes in the saturation were observed (compare Step I1 in Figure 9 with Step D13 in Figure 8). As the imbibition process progressed further, and when the advancing contact angles were reached, the MTM interfaces invaded the oil-filled pore elements, from smallest to the largest, and displaced oil toward the outlet. Consequently, the changes in oil saturation with respect to reductions in capillary pressure became more pronounced. Meanwhile, the oil-water interfaces moved from the corners towards the center of pores until they met each other and instantaneously filled the pore/throat through snap-off events. This process continued as the water/oil fractional flow was increased until a residual oil saturation was established. As seen in Figure 9, the local capillary pressures of the imbibition process typically fall below the drainage capillary pressures, which is consistent with the current understanding of pore-scale displacement physics. The difference between the two curves was smaller than expected, which could be attributed to the previous observation that interface relaxation does not allow the local capillary pressure to sufficiently increase during the drainage process. It should also be re-emphasized that the local capillary pressures were measured for the non-wetting phase clusters connected to the inlet of the FOV. At the late stages of the imbibition test, most of the remaining oil was trapped and it was not practical to measure the local capillary pressures.

3.4. Core-flooding experiments: wettability characterization

The sub-volumes of the segmented micro-scale images were also analyzed using the ACAM platform to characterize the wettability of the system. Thousands of contact angles were measured at the triple (i.e., fluid-fluid-solid) contact points in four sub-volumes cropped from one of the image sets obtained during the imbibition experiment. These measurements were then examined based on the acceptance criteria explained in section 2.2.2. The statistics of contact angle measurements for each of the sub-volumes are summarized in Table 2. As seen, the data generated for various sub-volumes are similar, which supports the reproducibility of the data.

The automated contact angles are also compared with a set of manual measurements obtained for a similar rock/fluid system [8]. Figure 10 illustrates that even though the fluids used in the two studies are different (i.e., Soltrol 170 versus decalin), the results are comparable and have close average values while the automated measurement technique provides a much greater number of data points and is less time-consuming. Moreover, most of the contact angles in both cases lie within the range of 30-70 degrees, which confirms the water-wetness of Berea sandstone in the presence of mineral oil and brine. It is evident that the distribution of the automated contact angle covers a wider range compared to the manual measurements. This broader range is mainly attributed to the higher number of measurements in the former case which necessarily includes: (i) correct measurements which are missed due to the biased, selective nature of manual measurements, and (ii) incorrect measurements due to either performing automated measurements at poorly imaged interfaces or some numerical errors associated with applying the automated method to the complex images of natural porous media. The automated method also resulted in a small percentage of measurements that are unexpectedly high or low (for instance Figure S12). Visual inspection of some of these measurements indicated that these values were mainly obtained at the corners or pore/throat junctions. In future studies, the use of more robust acceptance criteria and advanced interface analyzing techniques (e.g., addressing pinned interfaces [45, 46] and employing the Neumann triangle[44] method) can be considered to further improve the efficacy of the automated in-situ contact angle measurement technique.

The automated method was also used to measure contact angles using subvolumes extracted from the same location of a drainage (D6) and imbibition (I15) images. Figure 10 exhibits the contact angle distributions obtained for both processes along with the manual measurements mentioned previously [8]. As can be observed, the receding contact angles are more/less frequent in the range of 0-35/35-70 degrees compared to the advancing contact angles. This dependency of contact angles on the flow process is referred to as contact angle hysteresis and is mostly attributed to the surface roughness, mineral heterogeneity, and the adsorption of solute on solid surfaces.

4. Conclusion and final remarks

In this study, we presented novel platforms for automated measurement of in-situ curvature and contact angles from pore-scale fluid occupancy maps of multiphase flow processes in the pore space of natural porous media. We validated this platform using a set of synthetic data as well as micro-CT images of multiple capillary rise experiments. Afterward, we applied the automated measurement approaches to micro-CT images of Berea sandstone, acquired during steady-state drainage and imbibition flow processes, to estimate local capillary pressures and characterize in-situ wettability. We also compared the image-based (local) capillary pressures to those obtained using a macro-scale porous membrane experiment and presented new insights pertinent to the differences between the micro- and macro-scale measurements. The concluding remarks of this study are:

- The automatically measured curvatures of synthetic surfaces agreed well with the corresponding analytical values, especially for adequately large interfaces. Higher uncertainties, however, are associated with small interfaces which are represented by only a few voxels.

- The capillary pressures obtained from curvature analysis during the capillary rise experiments were consistent with the corresponding estimates obtained using the capillary height.

- Optimizing the interface smoothing parameters and eliminating some of the wetting layers and the vertices located at or near the triple contact points[22, 18, 36] allowed us to minimize the uncertainties associated with capillary pressure measurements when the image analysis platform was applied to complex micro-CT images of natural rock samples.

- The image-based capillary pressures computed during the drainage process correlated well with the macroscopic capillary pressure-saturation function. In some saturation ranges, however, pore-scale displacement events, such as Haines jump[43] and interface relaxation, caused some fluctuations in the capillary pressures and contributed to the discrepancies between the two functions.

- At the later stages of the drainage process, when the arc menisci movement governed the flow dynamics, only slight changes in saturations were observed with sharp increases in both the in-situ and macro-scale capillary pressures were found.

- The in-situ capillary pressures dropped significantly during the first step of the imbibition process. This was an indication of relaxation and hinging of the oil-water interfaces and it followed the trend predicted based on the relevant pore-scale displacement physics.

- Selective measurements should be performed based on certain acceptance criteria that automatically exclude measured contact angles when there is insufficient contact between the phases.

- Wettability characterization using the automated in-situ contact angle method demonstrated consistent results at different locations of the field of view. The data were also in agreement with the manual measurements reported in the literature[8]. In addition, the automated method enabled us to differentiate between the advancing and receding contact angles.

The developed automated curvature and contact angle measurement platforms represent powerful technologies to generate in-situ wettability and characteristics for multiphase flow through porous media. In future studies, these platforms can be further developed and applied to other flow processes and rock-fluid systems.

Acknowledgments

We gratefully acknowledge the financial support of Thermo Fisher Scientific, Hess Corporation, and the University of Wyoming. We express our appreciation to Dr. Bradley William McCaskill of Piri Research Group at the Center of Innovation for Flow through Porous Media for his insightful comments on the careful review of the manuscript. We also extend our gratitude to Evan Lowry of Pentair Flow & Filtration Solutions for his insights and constructive comments.

References

[1] P. Laplace, Supplements to the tenth edition, Mécanique céleste (1806).

[2] T. Young, An essay on the cohesion of fluids, Philosophical Transactions of the Royal Society of London 95 (1805) 65–87.

[3] W. Anderson, Wettability literature survey - part 2: Wettability measurement, Journal of Petroleum Technology 38 (1986) 1246–1262. doi:10.2118/13933-pa.

[4] G. Hassler, E. Brunner, Measurement of capillary pressures in small core samples, Trans. AIME 160 (1945) 114–123. doi:10.2118/945114-g.

[5] M. Leverett, Capillary behavior in porous solids, Trans. ASME 168 (1941) 129–139. doi:10.1515/crll.1958.200.129.

[6] W. Purcell, Capillary pressures - their measurement using mercury and the calculation of permeability therefrom, Journal of Petroleum Technology 1 (1949) 39–48. doi:10.2118/949039-g.

[7] M. Andrew, B. Bijeljic, M. Blunt, Pore-scale contact angle measurements at reservoir conditions using x-ray microtomography, Advances in Water Resources 68 (2014) 24–31. doi:10.1016/j.advAnwatres.2014.02.014.

[8] M. Khishvand, A. Alizadeh, M. Piri, In-situ characterization of wettability and pore-scale displacements during two- and three-phase flow in natural porous media, Advances in Water Resources 97 (2016) 279–298. doi:10.1016/j.advwatres.2016.10.009.

[9] P. Lv, Y. Liu, Z. Wang, S. Liu, L. Jiang, J. Chen, Y. Song, In situ local contact angle measurement in a CO2-brine-sand system using microfocused x-ray ct, Langmuir 33 (2017) 3358–3366. doi:10.1021/acs.langmuir.6b04533.

[10] M. Khishvand, A. H. Alizadeh, I. Oraki Kohshour, M. Piri, R. S. Prasad, In situ characterization of wettability alteration and displacement mechanisms governing recovery enhancement due to low-salinity waterflooding, Water Resources Research 53 (2017) 4427–4443. doi:10.1002/2016WR020191.

[11] Y. Xie, M. Khishvand, M. Piri, Impact of connate brine chemistry on in situ wettability and oil recovery: Pore-scale experimental investigation, Energy & Fuels 34 (2020) 4031–4045. doi:10.1021/acs.energyfuels.9b03787.

[12] K. A. Klise, D. Moriarty, H. Yoon, Z. Karpyn, Automated contact angle estimation for three-dimensional x-ray microtomography data, Advances in Water Resources 95 (2016) 152–160. doi:10.1016/j.advwatres.2015.11.006.

[13] A. Scanziani, K. Singh, M. J. Blunt, A. Guadagnini, Automatic method for estimation of in situ effective contact angle from x-ray micro tomography images of two-phase flow in porous media, Journal of Colloid and Interface Science 496 (2017) 51–59. doi:10.1016/j.jcis.2017.02.005.

[14] A. Ibekwe, D. Pokrajac, Y. Tanino, Automated extraction of in situ contact angles from micro-computed tomography images of porous media, Computers & Geosciences 137 (2020). doi:https://doi.org/10.1016/j.cageo.2020.104425.

[15] A. AlRatrout, A. Q. Raeini, B. Bijeljic, M. J. Blunt, Automatic measurement of contact angle in pore-space images, Advances in Water Resources 109 (2017) 158–169. doi:10.1016/j.advwatres.2017.07.018.

[16] J. Yang, Y. Zhou, An automatic in situ contact angle determination based on level set method, Water Resources Research 56 (2020). doi:https://doi.org/10.1029/2020WR027107.

[17] R. T. Armstrong, M. L. Porter, D. Wildenschild, Linking pore-scale interfacial curvature to column-scale capillary pressure, Advances in Water Resources 46 (2012) 55–62. doi:10.1016/j.advwatres.2012.05.009.

[18] C. Garing, J. A. de Chalendar, M. Voltolini, J. B. Ajo-Franklin, S. M. Benson, Pore-scale capillary pressure analysis using multi-scale x-ray micromotography, Advances in Water Resources 104 (2017) 223–241. doi:10.1016/j.advwatres.2017.04.006.

[19] A. L. Herring, J. Middleton, R. Walsh, A. Kingston, A. Sheppard, Flow rate impacts on capillary pressure and interface curvature of connected and disconnected fluid phases during multiphase flow in sandstone, Advances in Water Resources 107 (2017) 460–469. doi:10.1016/j.advwatres.2017.05.011.

[20] A. M. Alhammadi, Y. Gao, T. Akai, M. J. Blunt, B. Bijeljic, Pore-scale x-ray imaging with measurement of relative permeability, capillary pressure

and oil recovery in a mixed-wet micro-porous carbonate reservoir rock, Fuel 268 (2020). doi:https://doi.org/10.1016/j.fuel.2020.117018.

[21] M. Rucker, W.-B. Bartels, G. Garfi, M. Shams, T. Bultreys, M. Boone, S. Pieterse, G. Maitland, S. Krevor, V. Cnudde, H. Mahani, S. Berg, A. Georgiadis, P. Luckham, Relationship between wetting and capillary pressure in a crude oil/brine/rock system: From nano-scale to core-scale, Journal of Colloid and Interface Science 562 (2020) 159–169. doi:https://doi.org/10.1016/j.jcis.2019.11.086.

[22] T. Li, S. Schlter, M. I. Dragila, D. Wildenschild, An improved method for estimating capillary pressure from 3d microtomography images and its application to the study of disconnected nonwetting phase, Advances in Water Resources 114 (2018) 249–260. doi:10.1016/j.advwatres.2018.02.012.

[23] Q. Lin, B. Bijeljic, S. Berg, R. Pini, M. J. Blunt, S. Krevor, Minimal surfaces in porous media: Pore-scale imaging of multiphase flow in an altered-wettability bentheimer sandstone, Physical Review E 99 (2019). doi:10.1103/PhysRevE.99.063105.

[24] M. Heshmati, M. Piri, Experimental investigation of dynamic contact angle and capillary rise in tubes with circular and noncircular cross sections, Langmuir 30 (2014) 14151–14162. doi:10.1021/la501724y.

[25] A. Mohamed, M. Khishvand, M. Piri, A pore-scale experimental investigation of process-dependent capillary desaturation, Advances in Water Resources 144 (2020). doi:https://doi.org/10.1016/j.advwatres.2020.103702.

[26] A. H. Alizadeh, M. Piri, The effect of saturation history on three-phase relative permeability: An experimental study, Water Resources Research 50 (2) (2014) 1636–1664. doi:10.1002/2013WR014914.

[27] S. Rusinkiewicz, Estimating curvatures and their derivatives on triangle meshes, in: Proceedings. 2nd International Symposium on 3D Data Processing, Visualization and Transmission, 2004, pp. 486–493. doi:10.1109/TDPVT.2004.1335277.

[28] W. E. Lorensen, H. E. Cline, Marching cubes: A high resolution 3d surface construction algorithm, Association for Computing Machinery, New York, NY, USA, 1987. doi:10.1145/37401.37422.

[29] M. Desbrun, M. Meyer, P. Schröder, A. H. Barr, Implicit fairing of irregular meshes using diffusion and curvature flow, ACM Press/Addison-Wesley Publishing Co., 1999, pp. 317–324. doi:10.1145/311535.311576.

[30] D. Kroon, Smooth triangulated mesh, Matlab central file exchange (2021). URL https://www.mathworks.com/matlabcentral/fileexchange/26710-smooth-triangulated-mesh

[31] Y. Ben Shabat, A. Fischer, Design of porous micro-structures using curvature analysis for additive-manufacturing, Procedia CIRP 36 (2015) 279–284. doi:10.1016/j.procir.2015.01.057.

[32] E. Vouga, Lectures in discrete differential geometry 3 discrete surfaces (2014).

[33] K. Crane, Discrete differential geometry: An applied introduction., Course notes, Carnegie Mellon University (2018).
URL www.cs.cmu.edu/~kmcrane/Proj.11

[34] L. Siqveland, S. M. Skjæveland, Derivations of the young-laplace equation, Vol. 339, N. Engl. J. Med., 1998, pp. 1725–1733. doi:10.13140/RG.2.1.4485.5768.

[35] K. Wardle, Differential Geometry, Dover Publication, 1965.

[36] T. Akai, Q. Lin, A. Alhosani, B. Bijeljic, M. J. Blunt, Quantification of uncertainty and best practice in computing interfacial curvature from complex pore space images, Materials 12 (2019). doi:10.3390/ma12132138.

[37] M. Piri, M. J. Blunt, Three-phase threshold capillary pressures in noncircular capillary tubes with different wettabilities including contact angle hysteresis, Phys. Rev. E 70 (2004). doi:10.1103/PhysRevE.70.061603.

[38] B. Raeesi, N. R. Morrow, G. Mason, Capillary pressure hysteresis behavior of three sandstones measured with a multistep outflowinflow apparatus, Vadose Zone Journal 13 (2014). doi:10.2136/vzj2013.06.0097.

[39] S. Holocombe, Splitfv - split a mesh, Matlab central file exchange (2021). URL https://www.mathworks.com/matlabcentral/fileexchange/27667-splitfv-split-a-mesh

[40] The MathWorks Inc. . MATLAB and Parallel Computing Toolbox. (2021a).

[41] The MathWorks Inc. . MATLAB and MEX File Functions. (2021a).

[42] W. B. Haines, Studies in the physical properties of soil. v. the hysteresis effect in capillary properties, and the modes of moisture distribution associated therewith, The Journal of Agricultural Science 20 (1930) 97116. doi:10.1017/S002185960008864X.

[43] S. Berg, H. Ott, S. A. Klapp, A. Schwing, R. Neiteler, N. Brussee, A. Makurat, L. Leu, F. Enzmann, J.-O. Schwarz, M. Kersten, S. Irvine, M. Stampanoni, Real-time 3d imaging of haines jumps in porous media flow, Proceedings of the National Academy of Sciences 110 (2013) 3755–3759. doi:10.1073/pnas.1221373110.

[44] R. David, S. M. Dobson, Z. Tavassoli, M. G. Cabezas, A. W. Neumann, Investigation of the neumann triangle for dodecane liquid lenses on water, Colloids and Surfaces A: Physicochemical and Engineering Aspects 333 (1) (2009) 12–18. doi:https://doi.org/10.1016/j.colsurfa.2008.09.018.

[45] M. J. Blunt, Q. Lin, T. Akai, B. Bijeljic, A thermodynamically consistent characterization of wettability in porous media using high-resolution imag-

ing, Journal of Colloid and Interface Science 552 (2019) 59–65. doi:https://doi.org/10.1016/j.jcis.2019.05.026.

[46] A. Mascini, V. Cnudde, T. Bultreys, Event-based contact angle measurements inside porous media using time-resolved micro-computed tomography, Journal of Colloid and Interface Science 572 (2020) 354–363. doi:https://doi.org/10.1016/j.jcis.2020.03.099.

[47] M. Arshadi, M. Khishvand, A. Aghaei, M. Piri, G. A. Al-Muntasheri, Pore-scale experimental investigation of two-phase flow through fractured porous media, Water Resources Research 54 (2018) 3602–3631. doi:10.1029/2018WR022540.

Tables and Figures

Table 1: Composition and physical properties of the liquid phases used in the capillary rise experiments. The density and IFT values were measured at ambient pressure and 21°C temperature.

Experiment	Liquid phase	Density (g/cm^3)	Surface tension (mN/m)
1	Distilled water + sodium iodide (10 wt.%)	1.078	67.04 ± 0.50
2	Glycerol + distilled water (27 wt.%) + potassium iodide (19 wt.%)	1.304	55.09 ± 0.14
3	Soltrol 170 + 1-iodooctane (15 wt.%)	0.851	22.51 ± 0.02

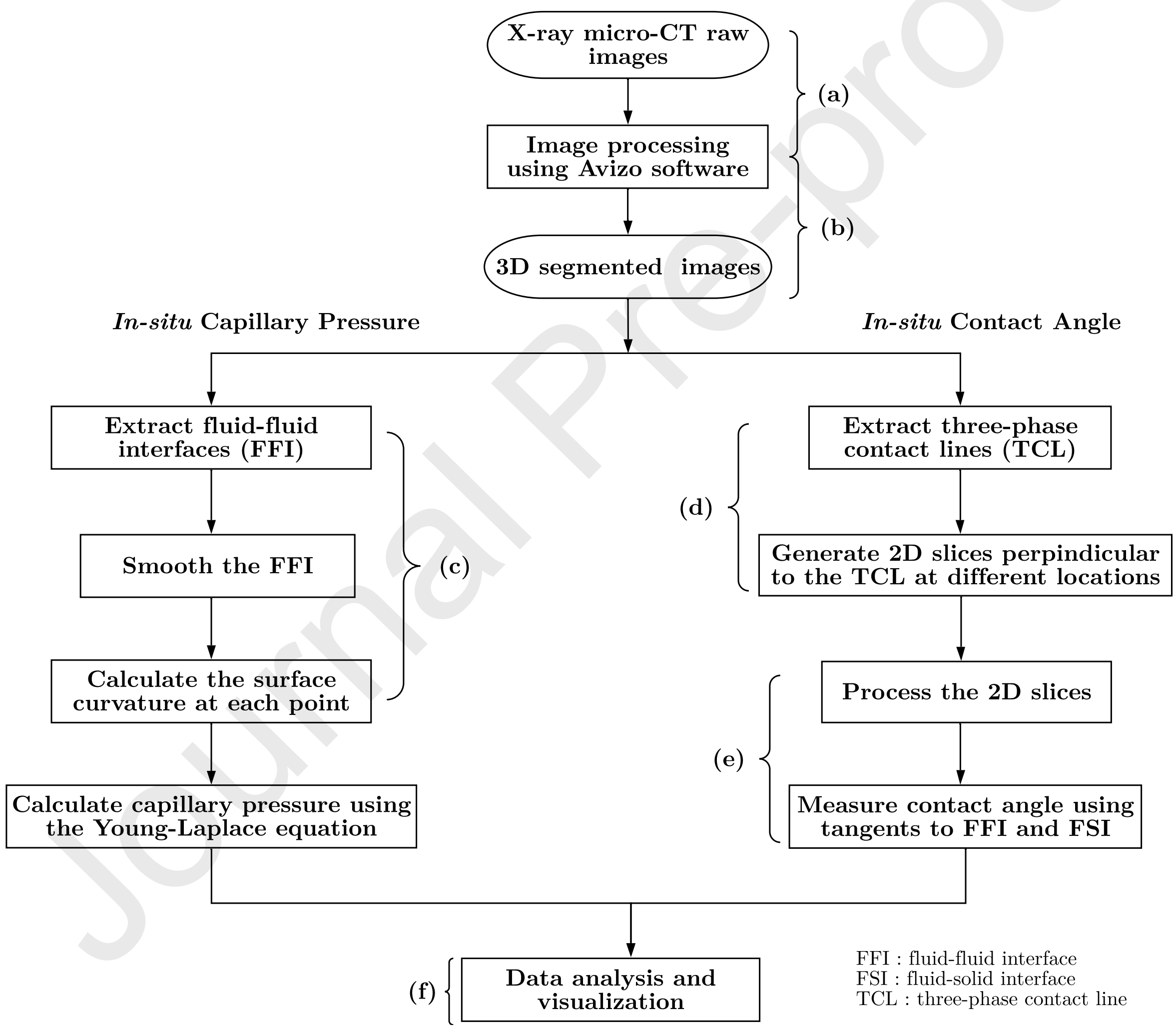

Figure 1: Flowchart of the image processing steps taken to measure capillary pressures and contact angles from micro-CT images. An example of each major step (i.e., a to f) is presented in Figure S3.

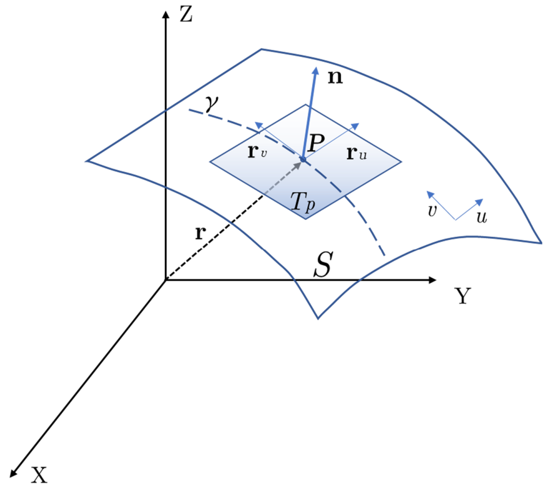

Figure 2: Schematic of the surface S in the 3D space and its geometrical parameters.

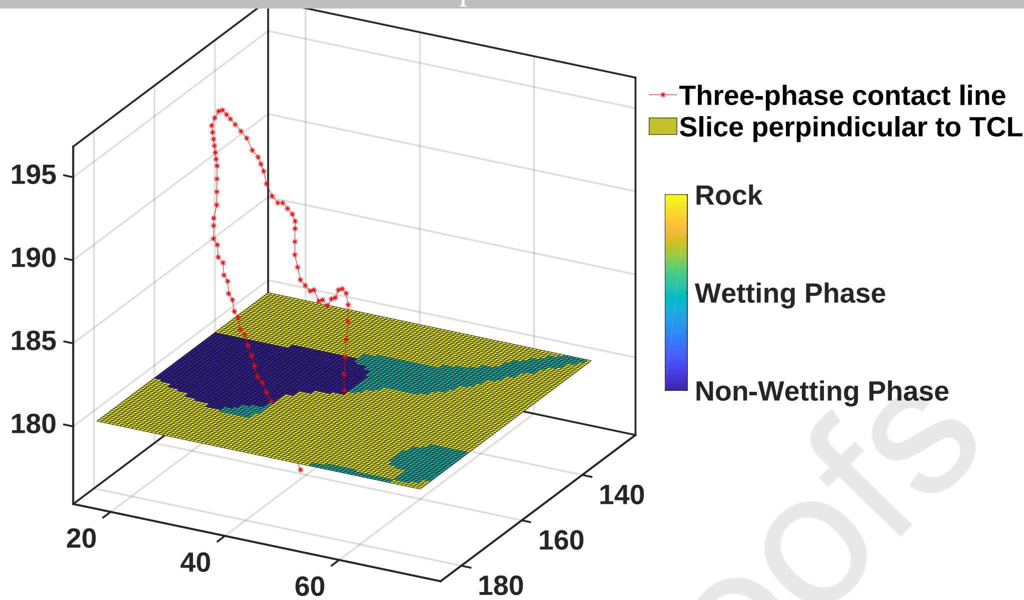

(a)

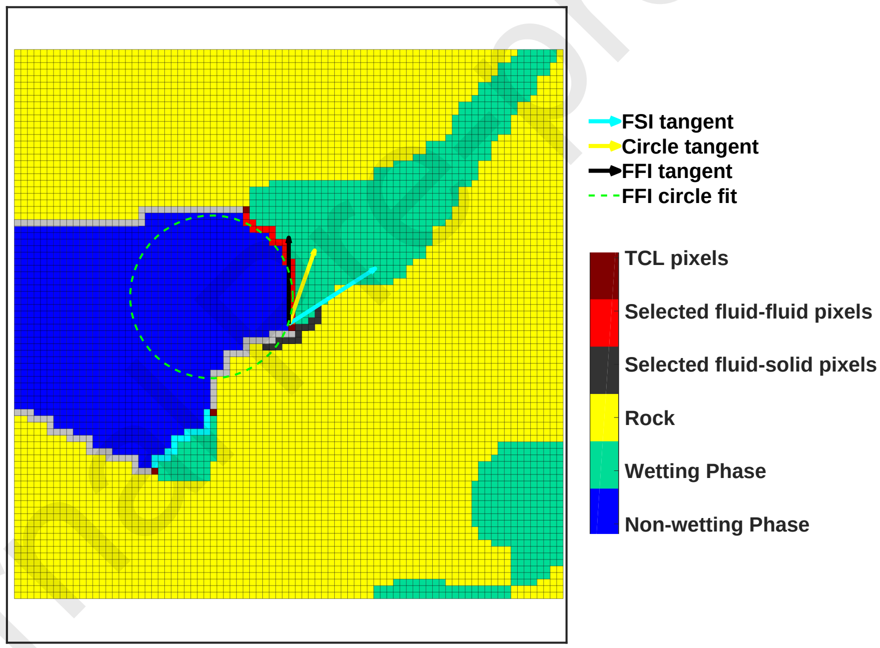

(b)

Figure 3: (a) The 2D slice perpendicular to the TCL at a specific point, and (b) the image processing technique to measure the contact angle between the FFI and the FSI (image resolution = 2μm).

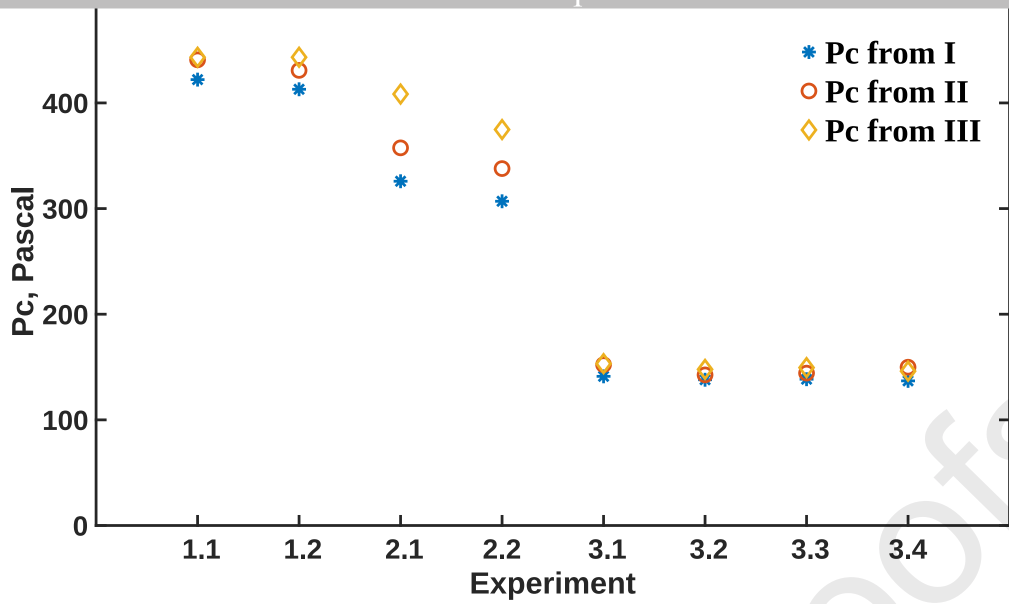

Figure 4: The comparison between curvature-based (i.e., formulas (I) and (II)) and hydrostatic pressure-based (formula (III)) capillary pressures during the capillary rise experiments. All formulas are shown in Equation(7).

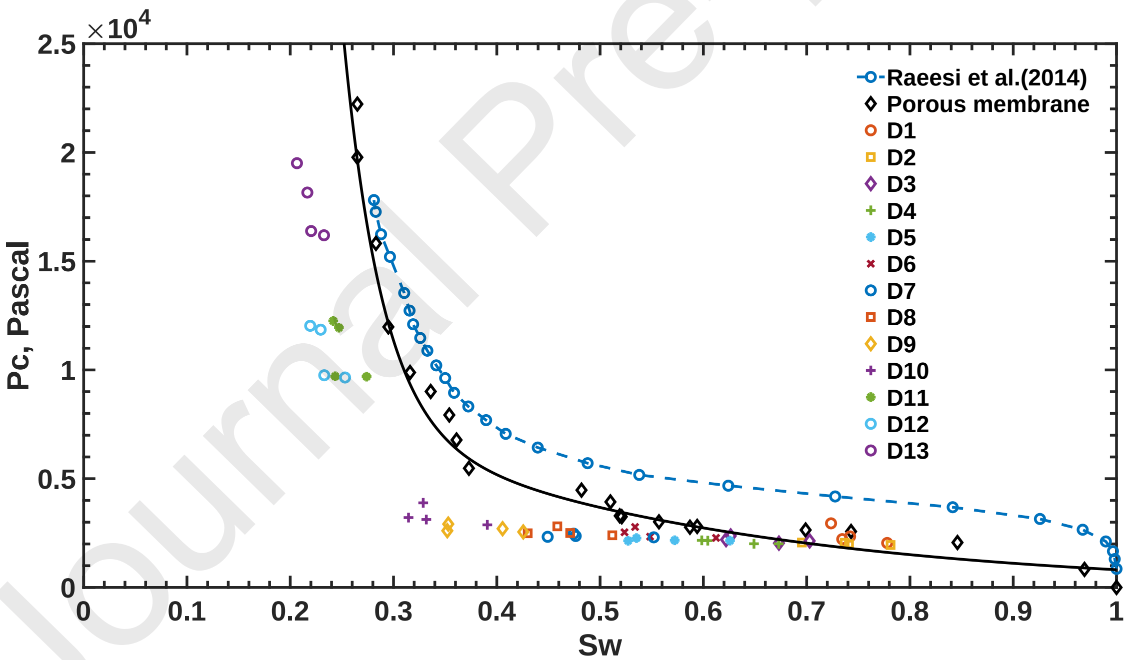

Figure 5: Comparison between the image-based capillary pressure - saturation relationship of various sub-volumes at different stages of the drainage experiment (D1-D13, see Table 4 in the SI) with the macroscopic functions obtained from porous membrane experiments conducted in this study and in a previous one[38]. The oil-brine interfacial tension in the micro-scale study was assumed to be consistent with the macro-scale system, i.e., 41.3 mN/m [47].

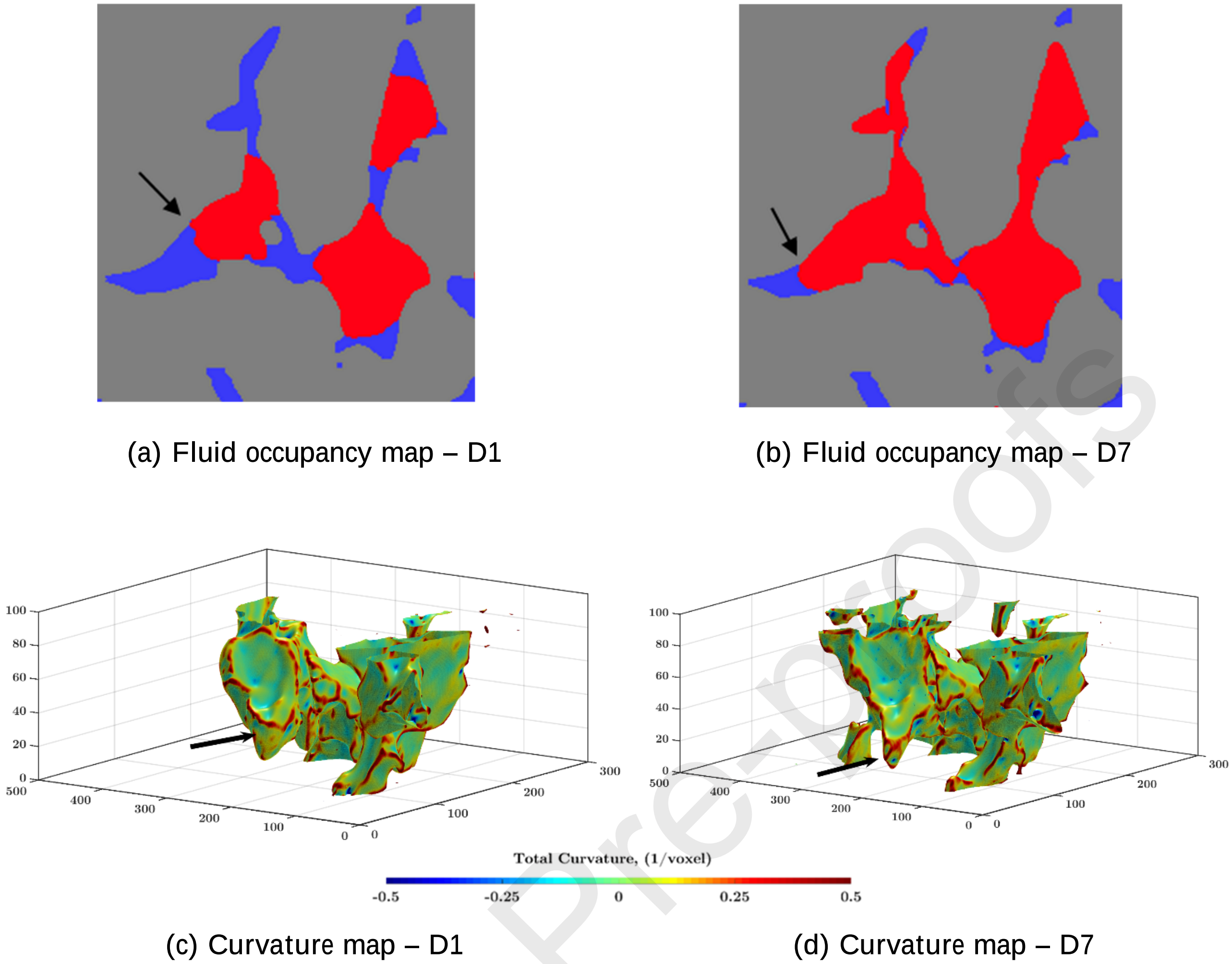

Figure 6: Fluid occupancy map and per-vertex computed curvature for a sub-volume when progressing from drainage process D1 to D7. The arrows indicate a location at which the local curvature (i.e., capillary pressure) increases due to the movement of fluid-fluid interfaces toward narrower corners (image resolution = 2μm).

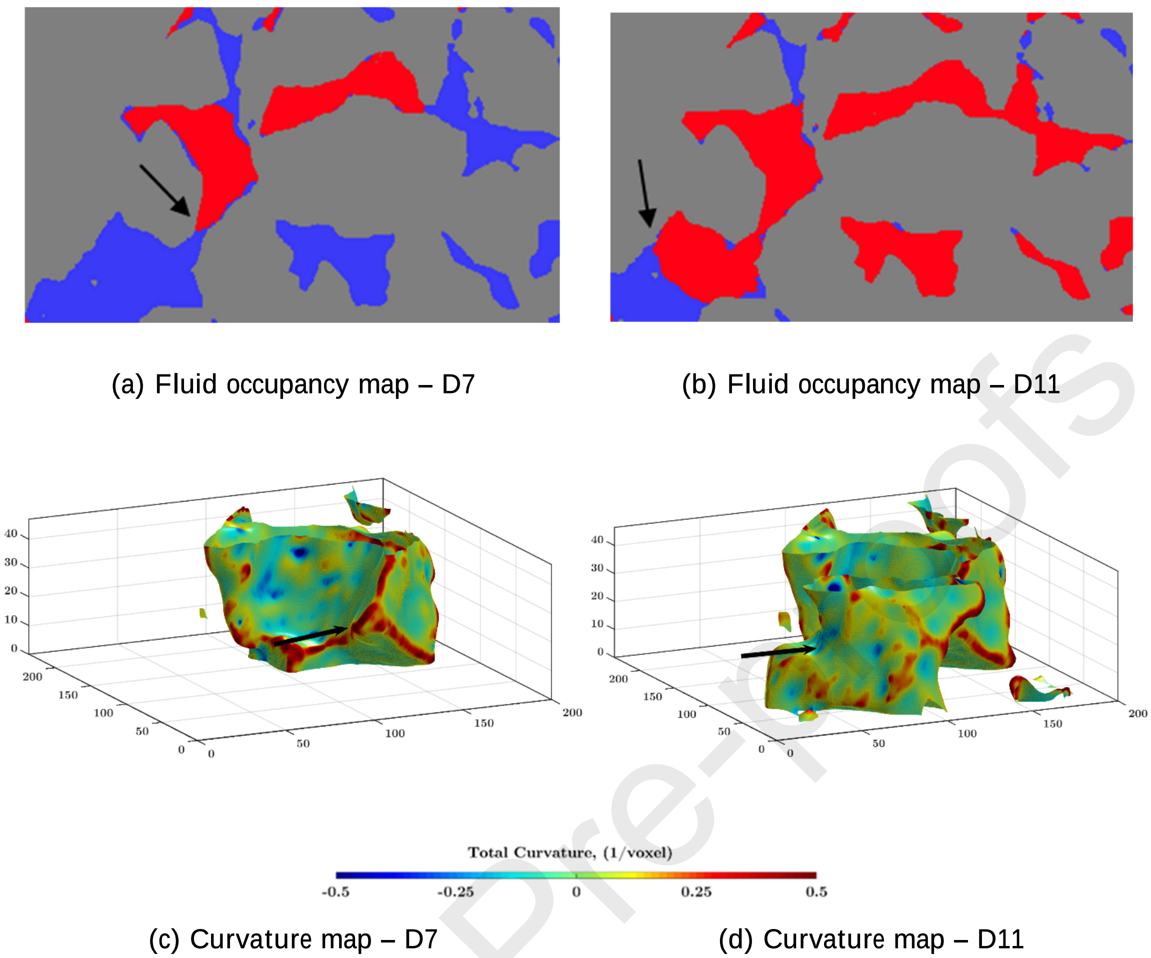

(a) Fluid occupancy map – D7

(b) Fluid occupancy map – D11

(c) Curvature map – D7

(d) Curvature map – D11

Figure 7: Fluid occupancy map and per-vertex computed curvature for a sub-volume when progressing from drainage process D7 to D11. The arrows indicate curvature relaxation due to the movement of interfaces from a narrow throat to a larger pore (image resolution $= 2\mu$m).

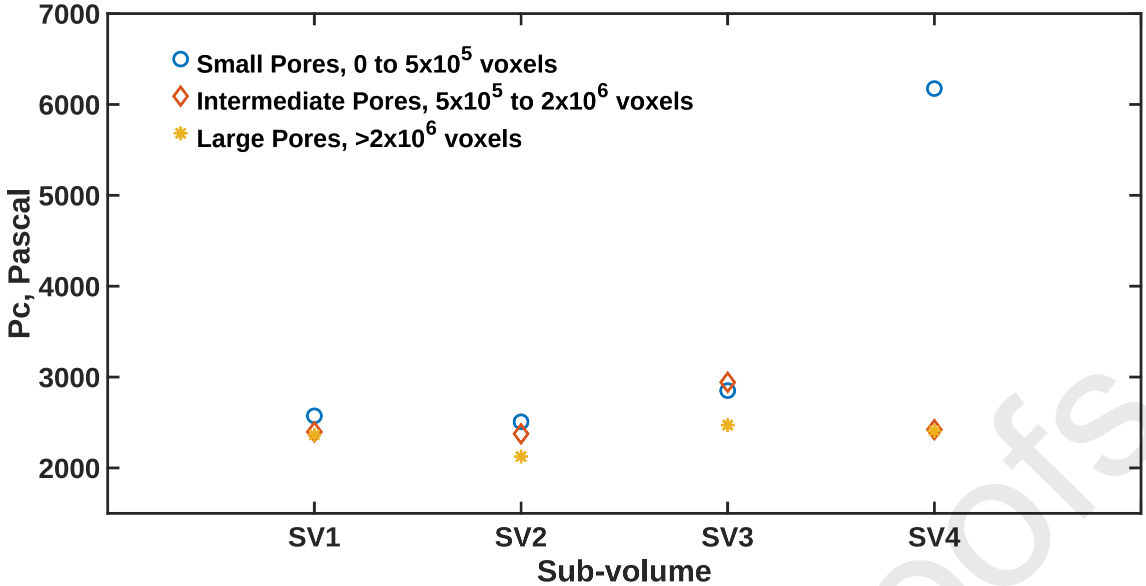

Figure 8: Local capillary pressures in different pore sizes during the drainage process D7.

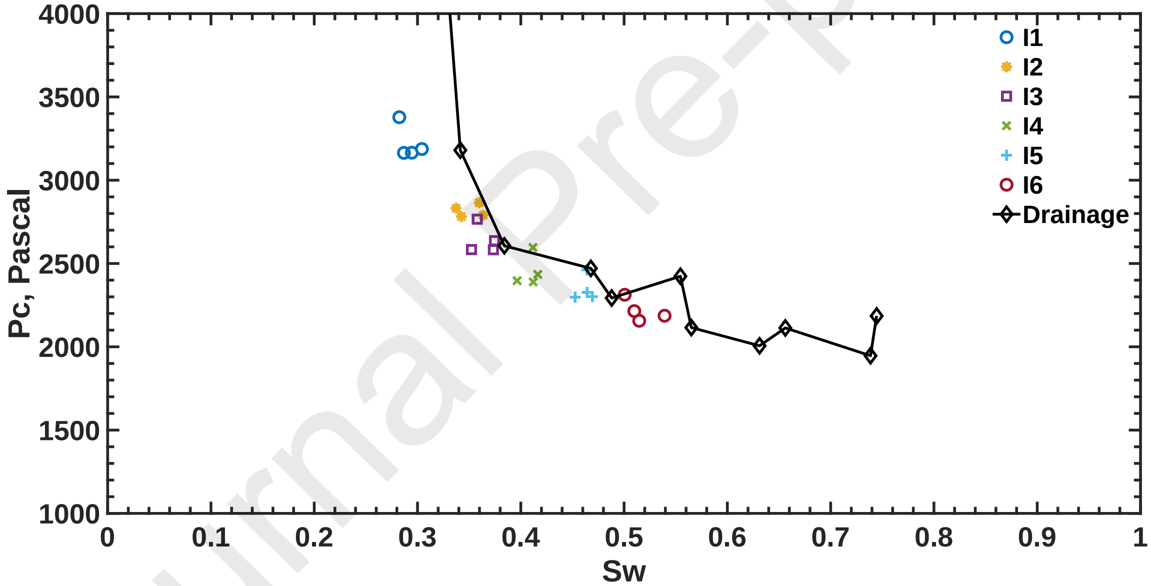

Figure 9: Image-based capillary pressure vs. saturation relationship during the imbibition (I) process. The markers show the average capillary pressure in various sub-volumes. The jaggedness observed in the drainage data is attributed to the successive build-up and relaxation of the interfacial curvature associated with type (iii) displacements.

Table 2: Summary of the automated contact angle measurements for four sub-volumes cropped from the segmented image of one of the imbibition processes.

Sub-volume	Sub-volume size (voxels)	Total number of measurements	Accepted measurements	Average contact angle (degrees)
SV1	252x245x101	9782	5222	47.7 ± 21.8
SV2	225x284x56	6355	3682	48.1 ± 18.8
SV3	420x147x51	4804	2395	47.2 ± 19.8
SV4	352x156x51	4601	2564	53.3 ± 19.6
Total		25542	13863	48.8 ± 19.6

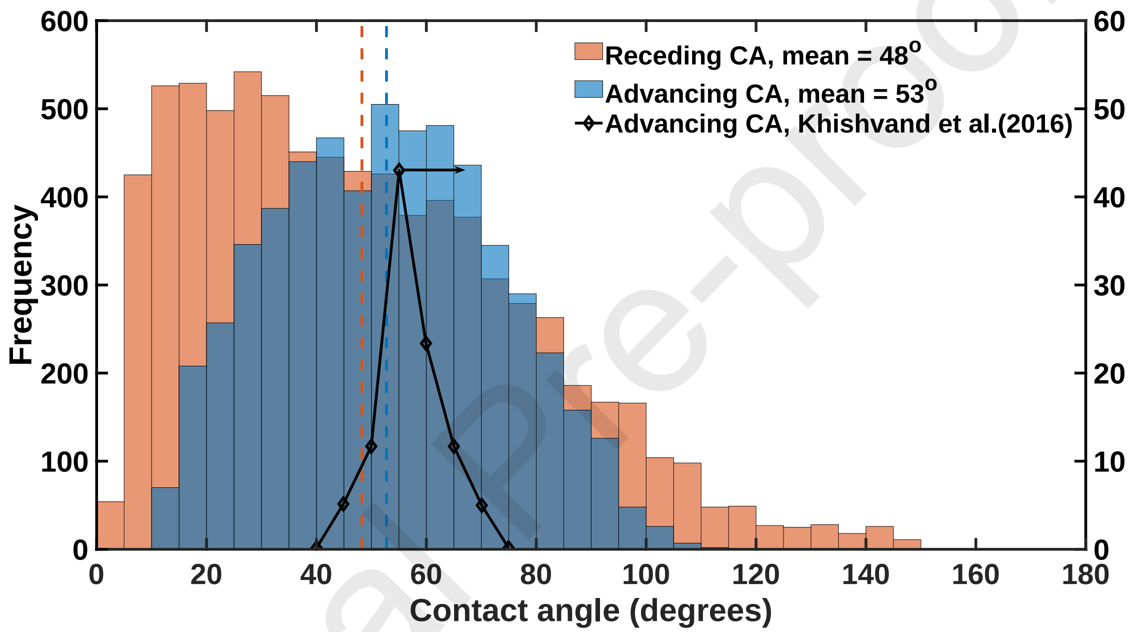

Figure 10: Comparison between the receding and advancing contact angles measured during the drainage and imbibition processes, respectively, along with the manual measurements in a similar study [8] for a water-wet Berea sandstone.